Survey of tungsten gross erosion from main plasma facing components in WEST during a L-mode high fluence campaign

N. Fedorczak, C. Arnas, L. Cappelli, L. Colas, Y. Corre, M. Diez, A. Gallo, J. Gaspar, A. Grosjean, C. Guillemaut, et al.

▶ **To cite this version:**

N. Fedorczak, C. Arnas, L. Cappelli, L. Colas, Y. Corre, et al.. Survey of tungsten gross erosion from main plasma facing components in WEST during a L-mode high fluence campaign. Nuclear Materials and Energy, 2024, 41 (4), pp.101758. 10.1016/j.nme.2024.101758 . cea-04816563

HAL Id: cea-04816563
https://cea.hal.science/cea-04816563v1

Submitted on 3 Dec 2024

HAL is a multi-disciplinary open access archive for the deposit and dissemination of scientific research documents, whether they are published or not. The documents may come from teaching and research institutions in France or abroad, or from public or private research centers.

L'archive ouverte pluridisciplinaire **HAL**, est destinée au dépôt et à la diffusion de documents scientifiques de niveau recherche, publiés ou non, émanant des établissements d'enseignement et de recherche français ou étrangers, des laboratoires publics ou privés.

Distributed under a Creative Commons Attribution 4.0 International License

Nuclear Materials and Energy 41 (2024) 101758

Contents lists available at ScienceDirect

Nuclear Materials and Energy

journal homepage: www.elsevier.com/locate/nme

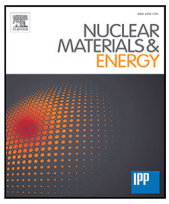

Survey of tungsten gross erosion from main plasma facing components in WEST during a L-mode high fluence campaign

N. Fedorczak [a,*], C. Arnas [d], L. Cappelli [b], L. Colas [a], Y. Corre [a], M. Diez [a], A. Gallo [a], J. Gaspar [c], A. Grosjean [e], C. Guillemaut [a], J.P. Gunn [a], C. Johnson [f], C. Martin [d], E. Tsitrone [a], E.A. Unterberg [f], J. Bucalossi [a], the WEST team [1]

[a] CEA, IRFM, F-13108 Saint-Paul-Lez-Durance, France
[b] M2P2 Aix-Marseille Univ, CNRS, Centrale Marseille, 13013 Marseille, France
[c] Aix Marseille Univ, CNRS, IUSTI, Marseille, France
[d] CNRS, Aix-Marseille universit'e, PIIM, 13397 Marseille, France
[e] University of Tennessee, Knoxville, TN 37996, United States of America
[f] Oak Ridge National Laboratory, Oak Ridge, TN 37831-6169, United States of America

ARTICLE INFO

Keywords:
Plasma material interaction
Tungsten erosion
Visible spectroscopy
Langmuir probe
high fluence exposure
WEST tokamak

ABSTRACT

An initial high fluence campaign was performed in WEST, in 2023, on the newly installed actively cooled tungsten divertor composed of ITER-grade monoblocks. The campaign consisted in the repetition of a 60 s long Deuterium L-mode pulse in attached divertor conditions, cumulating over 10000s of plasma exposure. A maximum deuterium fluence of approximately $5 \cdot 10^{26}$ m^{-2} was reached in the outer strike point region, representative of a few high performance ITER pulses. Gross tungsten erosion inferred from visible spectroscopy shows that the most eroded plasma facing component is the inner divertor target with rates ten times larger than on the outer divertor target. The outer midplane tungsten bumpers, located a few centimeters from the plasma, show gross erosion rates two times lower than at the outer divertor. We conclude that the outer midplane bumpers have a negligible contribution to the long range tungsten migration and deposition onto the lower divertor. The cumulated gross erosion rate on the inner divertor translates in an effective gross erosion thickness of about 20 μm, while it is about 2 μm for the outer divertor. Strikingly, these orderings coincide with the thickness of deposits found locally on the divertor: the exposed surfaces of high field side monoblocks are covered with several tens of μm tungsten deposits, while on the lower field side, few μm thin tungsten deposits are only found on the magnetically shadowed parts of monoblocks. The strong impact of those deposits on WEST operation, namely perturbation of surface temperature measurement with infra-red thermography, and the emission of flakes causing radiative perturbation of the confined plasma, calls for anticipating similar issues in ITER. In particular, the start of research operation shall consider the definition of a divertor erosion budget in order to anticipate the formation of deleterious deposits.

1. Introduction

The WEST tokamak has started its second phase of operation in end of 2022, with the installation of a fully actively cooled lower divertor composed of ITER grade tungsten monoblocks. Using lower hybrid current drive and heating, quasi steady-state pulses of several tens of seconds are commonly achieved, mostly in L-mode attached conditions with deuterium fuel. The first experimental campaign with this new divertor (so called C7 campaign taking place in 2023) covered about 6 h of plasma operation with the injection of about 40 GJ of radio-frequency power. The second half of this campaign was devoted to a so called high fluence deuterium experiment (see [1] for an overview of the scientific project) consisting in the repetition of a unique L-mode scenario, for 20 days and without boronisation [2], aiming at reaching ITER relevant particle fluence on the lower divertor. While ITER high performance operation will feature semi-detached divertor conditions [3], meaning a low eroding regime for tungsten monoblocks, the C7 WEST campaign consisted mostly in attached divertor conditions. As a matter of facts, the lower divertor showed progressive coverage by micrometer thick deposits over the C7 campaign, with a significant increase of deposit growth during the high fluence sessions.

* Correspondence to: Cadarache Center, Building 508, F-13108 Saint Paul Lez Durance, France.
E-mail address: nicolas.fedorczak@cea.fr (N. Fedorczak).
[1] See http://west.cea.fr/WESTteam.

https://doi.org/10.1016/j.nme.2024.101758
Received 25 June 2024; Received in revised form 19 September 2024; Accepted 4 October 2024
Available online 11 October 2024
2352-1791/© 2024 The Authors. Published by Elsevier Ltd. This is an open access article under the CC BY license (http://creativecommons.org/licenses/by/4.0/).

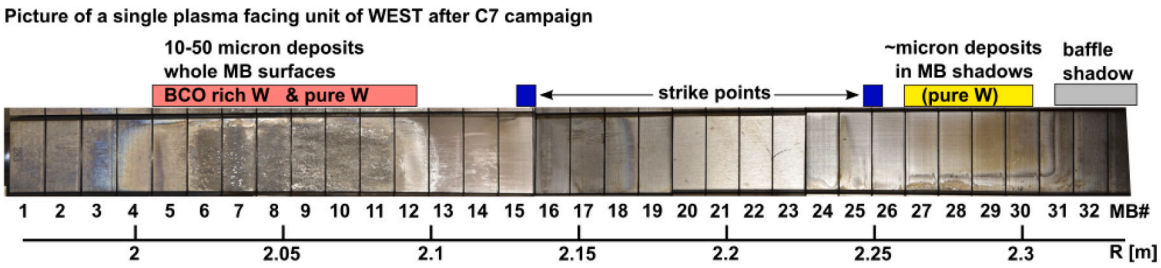

Fig. 1. Picture of a single plasma facing unit taken inside the tokamak after the (2023) C7 high fluence campaign. The two magnetic strike points of the high fluence scenario are indicated in blue. Monoblocks 1 to 19 compose the high field side or inner part, whereas monoblocks 24 to 33 compose the low field side or outer part of the divertor. Note that thick deposits on the high field side cover most of the monoblocks surfaces, whereas on the low field side thin deposits are only found in the magnetic shadow of individual monoblocks. (For interpretation of the references to color in this figure legend, the reader is referred to the web version of this article.)

The end of the campaign was hampered by regular emission of small flakes from the high field side area, causing radiative perturbation of the core plasma [4]. After the campaign, observations (Fig. 1) show that high field side far SOL area features several tens of μm (up to 50 μm) deposits [5] covering the exposed surface of monoblocks, consisting in dense tungsten dominated layers, together with oxygen and boron rich tungsten layers. Both high field side and low field side strike point areas are in principle net erosion zones, but shows micrometer (≈1–2 μm) thick pure tungsten deposits in the shadowed part of beveled monoblocks. Profilometry on divertor surface has not yet been achieved, such that net erosion areas are not yet known. In particular, the origin of very thick deposits of the high field side is not understood. The main plasma facing components are the divertor and the protection limiters of the two active lower hybrid current drive (LHCD) antennae. This report aims at compiling in-situ erosion data from these components during the high fluence campaign, and compare the magnitude of in-situ measurements to post-mortem observations.

2. Plasma scenario and diagnostics

Over 20 days of operation, about 380 pulses were performed, cumulating 3 h of plasma and 30 GJ of injected lower hybrid energy. The scenario, described on Fig. 2, consists in a L-mode plasma heated with 3.8 MW of LHCD, featuring 50% of total radiated power measured with bolometry [6]. Plasma current and density were optimized in order to maximize the time integrated particle flux measured on the outer strike point (see Fig. 4) while offering operation reliability and repeatability. As seen on Fig. 2, the L-mode phase is fairly stable for about 55 s. The outer strike point electron temperature (density) stays around 20 eV ($3 \cdot 10^{19}$ m^{-3}). The parallel deuterium ion flux (ion saturation flux) measured with Langmuir probes, projected on the beveled surface of monoblocks, gives a particle flux of about $6 \cdot 10^{22}$ m^{-2} s^{-1}. This flux, integrated over 10000S of plasma exposure, gives a campaign integrated fluence of $6 \cdot 10^{26}$ m^{-2}, in the range of several hundred seconds of ITER high performance conditions [3] (a few pulses). For comparison, the initial ASDEX-Upgrade campaign on a tungsten divertor [7] did cumulate about 2600s of plasma, with a deuterium fluence at the outer strike point of approximately $8 \cdot 10^{25}$ m^{-2}.

LHCD power is coupled to the plasma via two antennae located on the low field side, each protected by two side limiters made of actively cooled graphite coated with tungsten [8]. As shown on Fig. 3, the front face of these limiters is inclined with a 10 degree angle with respect to the toroidal direction, and are about 10 cm wide. Some of these limiters are monitored with multiple lines of sight of visible spectroscopy [9]. Two reciprocating Langmuir probes, located in a toroidally separated outboard limiter [10], will infer plasma density and temperature backgrounds in front of the limiters. The geometry of different diagnostics used in the following are shown on Fig. 3. In particular, the divertor conditions are inferred from flush mounted Langmuir probes and visible spectroscopy, as in other devices [11–13].

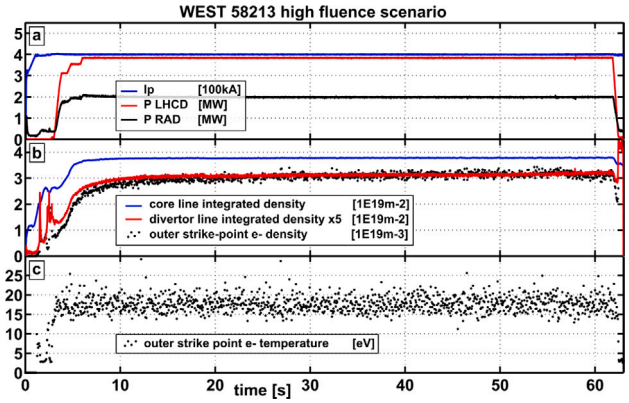

Fig. 2. Time traces of a representative plasma pulse from the High fluence campaign of 2023, lasting about 60 s. (a) Plasma current (blue), lower hybrid power coupled to the plasma (red), and total radiated power (black). (b) Time traces of core line integrated density (blue), divertor line integrated density ×5 (red) from interferometry, and outer strike point electron density measured by Langmuir probe (black dots). (c) Outer strike point electron temperature from Langmuir probe. (For interpretation of the references to color in this figure legend, the reader is referred to the web version of this article.)

Note that due to toroidal ripple, the divertor loads are toroidally modulated with high field side and low field side patterns out of shift [14]. High and low field side measurements are respectively located at the toroidal location of local ripple maxima. Note that the general pattern of ripple on WEST is consistent with the toroidally varying projection of toroidally uniform parallel fluxes [15].

3. Loads and erosion on plasma facing components

The repeated scenario shown on Fig. 2 allows us to build averaged profiles with accurate confidence intervals. For that purpose, a series of pulses are selected from the beginning of the campaign (no flaking impacting the scenario [4] and data are gathered from time intervals ranging from 20 s to 60 s (on the flat top of plasma density evolution). We can verify that the statistical distribution of local data (for instance electron density or temperature from a single probe) is very close to Gaussian. In all figures of the papers, errorbars are defined as a 95% confidence interval (or two times the standard deviation for a Gaussian).

Plasma conditions on the divertor are shown on Fig. 4, whereas conditions on the outboard antenna are pictured on Fig. 5. The divertor plasma is attached, with electron temperature ranging from about 10 eV in the far SOL up to 20 eV at both strike points. Note that the private flux region shows very scattered probe temperature data, because of very weak collected currents. Electron density is in the range of $3 \cdot 10^{19}$ m^{-3} at both strike points. The ion flux is more pronounced at the outer than the inner strike point (6 vs $4 \cdot 10^{22}$ m^{-2} s^{-1}).

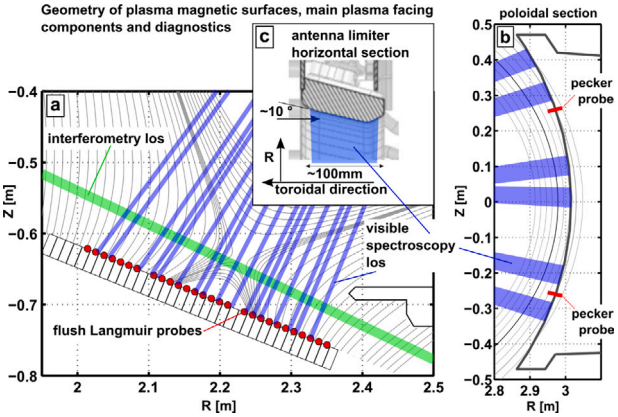

Fig. 3. (a) Poloidal cross section of the lower divertor geometry, showing the magnetic flux surfaces (gray curves), the line of sight of the divertor interferometry (green line), divertor monoblocks (white rectangles), the position of the Langmuir probes (red dots) and the lines of the sights of the visible spectroscopy (blue). (b) Zoom on the outer midplane, showing the contour of the LHCD antenna limiters, the lines of sights of the visible spectroscopy (blue) and the paths of peckers Langmuir probes installed on a movable outer limiter. (c) Horizontal cross section of the LHCD limiter, showing the visible spectroscopy coverage. (For interpretation of the references to color in this figure legend, the reader is referred to the web version of this article.)

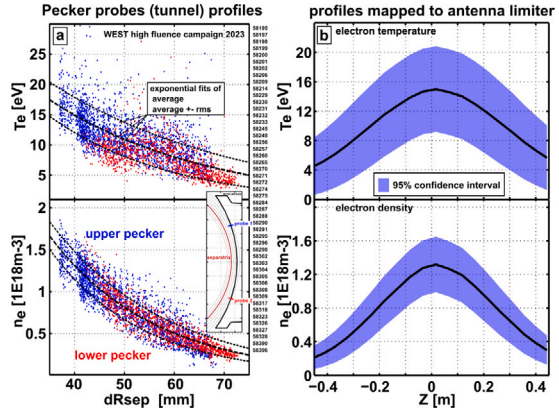

Fig. 5. Langmuir probe data from the two reciprocating pecker systems installed in a outer midplane movable limiter. (a) Electron temperature (top) and density (bottom) profiles, plotted as function of the distance to separatrix evaluated at outermidplane (dRsep). Note that the magnetic flux surfaces from equilibrium have been shifted down by 30 mm to match electron pressures from the two probes. The dashed curves represent exponential fits of the local mean data, plus or minus the standard deviation (evaluated on radial windows of 2 mm). (b) Profiles of electron temperature (top) and density (bottom) mapped from pecker probe to the poloidal contour of the LHCD limiters. The horizontal axis is the vertical position along the limiter. The colored error-bars represent the 95% confidence interval inferred from experimental profiles.

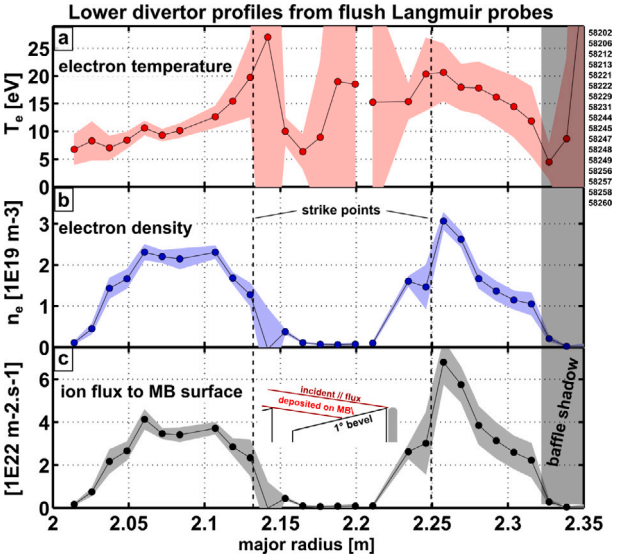

Fig. 4. Langmuir probe data from the lower divertor: (a) electron temperature, (b) electron density and (c) ion flux projected on the surface of beveled monoblocks. Data are averaged over a series of stable pulses from the beginning of the high fluence campaigns. Colored error-bars represent the 95% confidence interval computed from the data-set. The position of the two strike points is shown as dashed lines. On the right hand side, the portion of the divertor is in the magnetic shadow of the baffle (see Fig. 3).

The antenna limiters are subject to weaker plasma loads, as the antennae are positioned at the maximum distance from the plasma that ensures optimal wave coupling. The remapping of the two midplane reciprocating probes on the LHCD limiters are shown on Fig. 5: electron density is in the range of 10^{18} m^{-3} and electron temperature around 15 eV. It represents an ion flux deposited on the limiter surface (considering an incident angle of 10 degrees, see Fig. 3) of about $8 \cdot 10^{21}$ m^{-2} s^{-1}, that is seven times less than on the outer divertor strike point. Note that similar ratios can be reported from past ASDEX-Upgrade experiments [16].

In-situ tungsten gross erosion is measured with absolutely calibrated visible spectroscopy, focusing on the atomic line of neutral tungsten at $\lambda = 400.9$ nm [11–13,17]. For simplicity, a constant inverse photon efficiency $S/XB = 30$ is applied to transform the photon flux into neutral particle flux emitted by the surface. Note that experimentally inferred values of S/XB are in the range of 30 for an electron temperature of 20eV, and 20 for a temperature of 10eV [18]. Results are shown on Fig. 6 for both the lower divertor and a midplane LHCD limiter.

The outer target shows a gross flux in the range of 10^{19} m^{-2} s^{-1}, with a profile shape resembling the incident ion flux measured by Langmuir probe. The effective sputtering yield is in the range of $Y_{eff}^{lfs} \equiv \Gamma_W/\Gamma_D \approx 2 \cdot 10^{-4}$, which is coherent with the range of effective sputtering yields measured in the tungsten divertor of ASDEX-Upgrade and JET-ILW [11,19] for low-Z impurity concentrations below 1%. On the high field side divertor, spectroscopic measurements give a gross tungsten erosion reaching locally 10^{20} m^{-2} s^{-1}, so an order of magnitude larger than on the low field side. As the ion flux to the inner target is in the same range as to the outer target, it means that the effective sputtering yield at the inner target is an order of magnitude higher as well: $Y_{eff}^{hfs} \approx 2.5 \cdot 10^{-3}$. It can be verified on visible spectroscopy data that Boron, Carbon and Oxygen atomic lines are also an order of magnitude more intense from the inner target than the outer one, qualitatively consistent with the inner/outer asymmetry of the tungsten erosion. A precise description of the impurity mix responsible for tungsten erosion in this experiment is beyond the scope of this paper. The high field side far SOL seems to concentrate both low Z and high Z impurities. Spectroscopy from the outer antenna gives an estimate of gross tungsten erosion in the range of $5 \cdot 10^{18}$ m^{-2} s^{-1}, that corresponds to a effective sputtering yield of $Y_{eff}^{omp} \approx 6 \cdot 10^{-4}$. This yield is larger than estimated at the outer strike point, with no clear explanation for this observation at that stage. We can mention that the LHCD limiters, made of actively cooled graphite components coated with tungsten, are subject to very localized delaminated spots. This could enhance the local carbon concentration and therefore the effective tungsten sputtering.

These gross tungsten erosion rates from spectroscopy are now integrated over the duration of the high fluence campaign (approximately

ten thousands seconds). The resulting gross tungsten fluence – in particle per unit area p.m^{-2} – does not generally represent the net eroded thickness, because redeposition plays an important role for tungsten [7,11,20]. It corresponds to the upper bound of the net erosion, and will be called *virtual* eroded thickness. It is further assumed that $5 \cdot 10^{22}$p.m^{-2} represents one micrometer of tungsten thickness. These virtual gross eroded thicknesses are reported on the right axes of Fig. 6. We obtain that about 20 μm of gross erosion can virtually take place on the high field side, about 2 μm on the low field side, and about 1 μm on outboard limiters. Of course, part of this gross erosion is promptly redeposited through Larmor radius effects and pre-sheath electrostatic recall [21], and further redeposited by divertor screening and finally long range plasma migration. It means that gross erosion is very unlikely to effectively cumulate over time into a gross eroded thickness. The local (promptly) redeposited fraction along the different objects of interest is estimated using a recent model presented in [22]. Results are shown on Fig. 6: About 80% of local redeposition is predicted on divertor targets, similar to results from DIII-D [20], whereas it fall to about 20% on the outboard limiters. Note that the redeposition physics depends on the eroding species (charge and mass), which is not precisely known at this stage. To simplify, Nitrogen was considered as the only eroding species, and its charge was varied from +3 to +7, a range large enough to encompass possible variability from the choice of low-Z impurity species. Electron density and temperature are varies within their respective 95% confidence intervals, further assuming $T_i = 2T_e$ [23]. Overall, parametric variations of the redeposited fraction are rather limited compared to local absolute values. The antenna redeposition is weak because the electron density is rather weak: the mean free path of neutral tungsten is large compared to both the W1+ Larmor radius and magnetic pre-sheath width. In the divertor, the common belief is to consider large redeposition in the range of 95% or higher, slightly larger than estimated for these WEST conditions. It can be explained by the rather modest electron density in this scenario combined with the rather Large magnetic field of WEST (3.7T). Note that past ASDEX-Upgrade observations also point toward redeposited fractions around 80% in the divertor (comparing spectroscopy induced gross flux and net erosion measurement) [11].

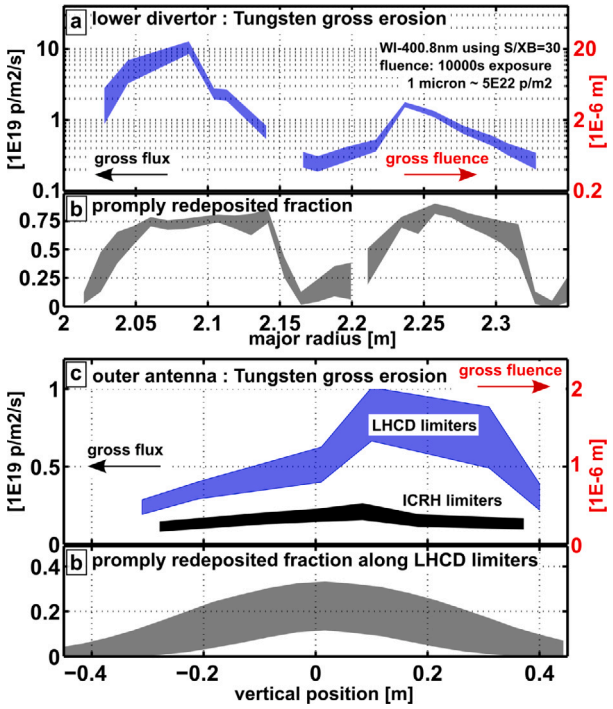

Fig. 6. Properties of Tungsten erosion from lower divertor and outer LHCD limiters. (a) gross erosion flux from visible spectroscopy on WI (400.8 nm) atomic line, using S/XB=30. The left vertical axis in an instantaneous gross flux estimate, averaged over the first part of the high fluence campaign (see Fig. 2 for pulse list). The vertical thickness of the curve represents the 95% confidence interval. The right vertical axis represents the same data transformed into a virtual gross eroded thickness, assuming a cumulative exposure of 10000s and considering that one micrometer of bulk tungsten represents about $5 \cdot 10^{22}$p/m^2. (b) Prompt redeposited fraction of the gross erosion, inferred from model [22], using data from Fig. 4. (c) Gross tungsten erosion along the LHCD limiters from visible spectroscopy on WI (400.8 nm) atomic line, using S/XB=30. For comparison is shown the data from a recessed ICRH limiter, showing that the LHCD limiters are the dominant equatorial sources. The right axis again shows a virtual cumulated thickness. (d) Prompt redeposition estimate using data from Fig. 5.

4. Tungsten balance

The high fluence scenario was run with the two lower hybrid antenna close to the plasma. We can assume that the 4 protection limiters receive approximately the same plasma load, and behave comparably in term of tungsten erosion. We will further assume that the erosion takes place over a vertical height of 0.5 m (Fig. 6) and a toroidal extent of 0.1 m (Fig. 3) per limiter. This gives a unitary limiter surface of $5 \cdot 10^{-2}$ m^2, or a total of midplane tungsten surface of 0.2m^2. Over this surface, we estimated a virtual gross erosion thickness of about 1 μm.

Note that WEST is also equipped with three ICRH antenna, with similar protection limiters. For plasma scenario heated with pure LHCD, these antennae are generally retracted five centimeters behind LHCD limiters, which was the case for the high fluence campaign. We can verify that the gross tungsten erosion from one of these ICRH limiter is indeed much lower than from the LHCD ones (Fig. 6), so that these specific sources can be disregarded.

The thick deposits of several tens of microns found on the high field side of WEST take place over approximately 7 monoblocks, or 8 cm of poloidal extend. The total deposit surface is therefore about 1 m^2. Note that the current post-mortem deposit studies suggest a toroidal modulation of the thicknesses, due to magnetic ripple, of about 50% [5], as also intuited by the toroidal modulation of infra-red emissivity and flaking probabilities [4]. Nevertheless, we can readily conclude that the antenna source cannot not cause the formation of high field side deposits: the total amount of gross tungsten erosion from the antenna (fluence times surface) is two orders of magnitude lower than both the equivalent metric from the divertor and the quantity found deposited on the high field side. This ratio is in line with what is reported in ASDEX-Upgrade [11].

On the other hand, it is striking to note that the virtual gross fluence estimated by visible spectroscopy in the divertor is in the range of deposit thicknesses measured after the campaign. On the low field side strike point area, deposits of a few microns are found on most of shadowed parts of monoblocks, whereas virtual gross fluence is about 2 μm. They could originate from local redeposition of the gross erosion from neighboring exposed surfaces of monoblocks. On the high field side, the virtual gross fluence of 20 μm is also coherent with the measured thickness of deposits. Note that the high fluence campaign is representing about half of the entire campaign, so numbers are in the same ball park, without trying to be more precise. Nevertheless, these thick deposits are not limited to the shadowed parts of monoblocks, but cover the exposed surfaces of those monoblocks. It is therefore puzzling to explain the growth of those deposits with local erosion phenomena.

In both cases, it means that net erosion areas need to be found on the monoblocks, to confirm a local redeposition patterns. Post-mortem analyses and profilometry are still under analyses while this paper is written.

5. Conclusion

The first high fluence campaign ran on WEST with the actively cooled tungsten monoblock divertor showed rapid formation of deposits on monoblock surfaces. In the high field side far SOL, thick

deposits of several tens of microns are observed, with portions rich in low-Z impurities (Boron–Oxygen–Carbon) and others being dense pure tungsten. In the low field side, deposits of a few micron thickness formed in the magnetic shadow of beveled monoblocks. Monitoring of gross erosion during experiments reveals that outer-midplane tungsten coated limiters (of lower hybrid antenna) are indeed eroded, but at a rate much lower than that required to explain the formation of those divertor deposits. On the contrary, gross erosion from the low field side divertor is coherent with the formation of micrometer thick deposits, whereas high field side erosion is coherent with tens of micrometer deposits. Both loaded divertor areas are characterized with estimated prompt reposition fraction in the range of 80%. It is not a complete proof that local erosion and redeposition is the dominant mechanism leading to the formation of these deposits, because it should be completed with post-mortem analyses of net erosion and redeposition patterns. Nevertheless, these initial observations from the first high fluence campaign with an ITER-grade divertor shall teach us that gross erosion may lead to the formation of deposits of equivalent thicknesses on nearby locations. It calls for the definition of a gross erosion budget for ITER. In particular, the start of research operation shall be considered carefully, because divertor conditions may not require partial detachment, and so tungsten erosion will eventually take place. The formation of tungsten deposits will occur, either on the shadow of beveled monoblocks, and possibly on the high field side far SOL. The fragility of these deposits is hampering plasma operation in WEST, and will probably in ITER at least by the modification of infra red surface emissivity and appearance of hot spots from delaminating flakes.

CRediT authorship contribution statement

N. Fedorczak: Writing – review & editing, Writing – original draft, Supervision, Investigation. **C. Arnas:** Validation, Investigation. **L. Cappelli:** Visualization, Validation, Software, Methodology. **L. Colas:** Validation, Investigation. **Y. Corre:** Validation, Supervision, Project administration. **M. Diez:** Validation, Methodology, Investigation. **A. Gallo:** Visualization, Validation, Methodology. **J. Gaspar:** Validation, Project administration, Investigation. **A. Grosjean:** Validation, Methodology. **C. Guillemaut:** Validation, Methodology, Data curation. **J.P. Gunn:** Validation, Methodology, Formal analysis, Data curation. **C. Johnson:** Validation, Methodology, Investigation. **C. Martin:** Validation, Methodology, Conceptualization. **E. Tsitrone:** Validation, Supervision, Project administration, Conceptualization. **E.A. Unterberg:** Validation, Project administration, Conceptualization.

Declaration of competing interest

The authors declare the following financial interests/personal relationships which may be considered as potential competing interests: Nicolas Fedorczak reports financial support was provided by European Consortium for the Development of Fusion Energy. If there are other authors, they declare that they have no known competing financial interests or personal relationships that could have appeared to influence the work reported in this paper.

Data availability

Data will be made available on request.

Acknowledgments

This work has been carried out within the framework of the EUROfusion Consortium, funded by the European Union via the Euratom Research and Training Programme (Grant Agreement No 101052200 — EUROfusion). Views and opinions expressed are however those of the author(s) only and do not necessarily reflect those of the European Union or the European Commission. Neither the European Union nor the European Commission can be held responsible for them.

References

[1] E. Tsitrone, et al., Overview of plasma wall interactions in the first high particle fluence campaign of WEST, Nucl. Mater. Energy (2024) this conference.
[2] A. Gallo, et al., Wall conditions in WEST during operations with a new ITER grade, actively cooled divertor, Nucl. Mater. Energy (2024) this conference.
[3] R.A. Pitts, X. Bonnin, F. Escourbiac, H. Frerichs, J.P. Gunn, T. Hirai, A.S. Kukushkin, E. Kaveeva, M.A. Miller, D. Moulton, V. Rozhansky, I. Senichenkov, E. Sytova, O. Schmitz, P.C. Stangeby, G. De Temmerman, I. Veselova, S. Wiesen, Physics basis for the first ITER tungsten divertor, Nucl. Mater. Energy 20 (2019) 100696.
[4] J. Gaspar, et al., Thermal and statistical analysis of the high-Z tungsten-based UFOs observed during the deuterium high fluence campaign of the WEST tokamak, Nucl. Mater. Energy (2024) this conference.
[5] C. Martin, et al., Post-mortem analysis of the deposit layers on the lower divertor after the high particle fluence campaign of WEST, Nucl. Mater. Energy (2024) this conference.
[6] P. Devynck, N. Fedorczak, R. Mao, S. Vartanian, WEST team, Calculation of the radiated power in WEST, J. Phys. Commun. 5 (9) (2021) 095008.
[7] M. Mayer, M. Andrzejczuk, R. Dux, E. Fortuna-Zalesna, A. Hakola, S. Koivuranta, K. Krieger, K.J. Kurzydlowski, J. Likonen, G. Matern, R. Neu, G. Ramos, M. Rasinski, V. Rohde, K. Sugiyama, A. Wiltner, W. Zielinski, ASDEX-Upgrade team, Tungsten erosion and redeposition in the all-tungsten divertor of ASDEX upgrade, Phys. Scr. 2009 (T138) (2009) 014039.
[8] M. Firdaouss, C. Desgranges, C. Hernandez, M. Richou, H. Greuner, B. Böswirth, I. Zacharie-Aubrun, T. Blay, J. Bucalossi, M. Missirlian, F. Samaille, E. Tsitrone, Overview of the different processes of tungsten coating implemented into WEST tokamak, Fusion Eng. Des. 124 (2017) 207–210, Proceedings of the 29th Symposium on Fusion Technology (SOFT-29) Prague, Czech Republic, September 5–9, 2016.
[9] O. Meyer, J.C. Giacalone, A. Gouin, J.Y. Pascal, C.C. Klepper, N. Fedorczak, Ph. Lotte, E.A. Unterberg, D.T. Fehling, J.H. Harris, WEST Team, Visible spectroscopy diagnostics for tungsten source assessment in the WEST tokamak: First measurements, Rev. Sci. Instrum. 89 (10) (2018) 10D105.
[10] J.P. Gunn, J.-Y. Pascal, A magnetically driven reciprocating probe for tokamak scrape-off layer measurements, Rev. Sci. Instrum. 82 (12) (2011) 123505.
[11] R. Dux, et al., Plasma-wall interaction and plasma behaviour in the non-boronised all tungsten {ASDEX} upgrade, J. Nucl. Mater. 390–39 (2009) 858–863.
[12] T. Abrams, R. Ding, H.Y. Guo, D.M. Thomas, C.P. Chrobak, D.L. Rudakov, A.G. McLean, E.A. Unterberg, A.R. Briesemeister, P.C. Stangeby, J.D. Elder, W.R. Wampler, J.G. Watkins, The inter-ELM tungsten erosion profile in DIII-D H-mode discharges and benchmarking with ERO+OEDGE modeling, Nucl. Fusion 57 (5) (2017) 056034.
[13] M. Tokitani, N. Yoshida, S. Masuzaki, N. Noda, A. Sagara, H. Yamada, A. Komori, S. Nagata, B. Tsuchiya, Plasma surface interaction on the surface of tungsten divertor tiles in LHD, J. Nucl. Mater. 415 (1, Supplement) (2011) S87–S91, Proceedings of the 19th International Conference on Plasma-Surface Interactions in Controlled Fusion.
[14] M. Firdaouss, T. Batal, J. Bucalossi, P. Languille, E. Nardon, M. Richou, Heat flux depositions on the WEST divertor and first wall components, Fusion Eng. Des. 98–99 (2015) 1294–1298, Proceedings of the 28th Symposium On Fusion Technology (SOFT-28).
[15] N. Fedorczak, J. Gaspar, M. Firdaouss, V. Moncada, A. Grosjean, R. Dejarnac, S. Brezinsek, E. Tsitrone, J. Bucalossi, T. Loarer, Infra-red thermography estimate of deposited heat load dynamics on the lower tungsten divertor of WEST, Phys. Scr. T171 (2020) 014046.
[16] R. Dux, ASDEX Upgrade Team, Main chamber sources and edge transport of tungsten in H-mode plasmas at ASDEX upgrade, Nucl. Fusion 51 (11) (2011) 119501.
[17] G.J. van Rooij, Olivier Meyer, S. Brezinsek, C. Desgranges, D. Douai, S. Ertmer, A. Gallo, C. Gil, J. Gunn, T. Loarer, E. Tsitrone, the EUROfusion PFC team, the WEST Team, Tungsten divertor sources in WEST related to impurity inventory and local plasma conditions, Phys. Scr. 2020 (T171) (2020) 014060.
[18] S. Brezinsek, M. Laengner, J.W. Coenen, M.G. O'Mullane, A. Pospieszczyk, G. Sergienko, U. Samm, Spectroscopic determination of inverse photon efficiencies of W atoms in the scrape-off layer of TEXTOR, Phys. Scr. 2017 (T170) (2017) 014052.
[19] G.J. van Rooij, et al., Tungsten divertor erosion in all metal devices: Lessons from the ITER like wall of JET, J. Nucl. Mater. 438, Supplement (2013) S42 – S47.
[20] R. Ding, D.L. Rudakov, P.C. Stangeby, W.R. Wampler, T. Abrams, S. Brezinsek, A. Briesemeister, I. Bykov, V.S. Chan, C.P. Chrobak, J.D. Elder, H.Y. Guo, J. Guterl, A. Kirschner, C.J. Lasnier, A.W. Leonard, M.A. Makowski, A.G. McLean, P.B. Snyder, D.M. Thomas, D. Tskhakaya, E.A. Unterberg, H.Q. Wang, J.G. Watkins, High-Z material erosion and its control in DIII-D carbon divertor, Nucl. Mater.

Energy 12 (2017) 247–252, Proceedings of the 22nd International Conference on Plasma Surface Interactions 2016, 22nd PSI.

[21] A.V. Chankin, D.P. Coster, R. Dux, Monte Carlo simulations of tungsten re-deposition at the divertor target, Plasma Phys. Control. Fusion 56 (2) (2014) 025003.

[22] L. Cappelli, N. Fedorczak, J.P. Gunn, S. Di Genova, J. Guterl, E. Serre, Study of the erosion and redeposition of W considering the kinetic energy distribution of incident ions through a semi-analytical model, Plasma Phys. Control. Fusion 65 (9) (2023) 095001.

[23] Y. Li, N. Fedorczak, G.S. Xu, Y. Liang, S. Brezinsek, J. Morales, The WEST Team, Effect of edge ion temperature on the divertor tungsten sputtering in WEST, Nucl. Fusion 63 (2) (2023) 026019.